Magnetic-Field-Induced Tunneling and Minigap Transport in Double Quantum Wells

S. K. Lyo, J. A. Simmons, N. E. Harff, T. M. Eiles, and J. F. Klem

Sandia National Laboratories, Albuquerque, NM 87185

Abstract. We review recent theoretical and experimental results on low-temperature tunneling and in-plane transport properties in double quantum wells (DQWs) in an in-plane magnetic field $\mathbf{B}_{||}$. These properties arise from the combined effect of $B_{||}$-induced relative displacement of the wave vectors in the two QWs and the interwell tunneling. In weakly coupled DQWs, the tunneling conductance has two sharp maxima as a function of $B_{||}$. In strongly coupled DQWs, a partial minigap is formed due to the anticrossing of the two QW dispersion curves, yielding sharp $B_{||}$-dependent structures in the density of states and in-plane transport properties. Excellent agreement is obtained between the theory and the data from GaAs/AlGaAs DQWs.

1. Introduction

In this paper, we discuss low-temperature tunneling and in-plane transport properties of double quantum wells (DQWs) in an in-plane magnetic field $\mathbf{B}_{||} \| \mathbf{x}$. DQWs consist of two parallel layers of two-dimensional (2D) degenerate electron-gases (2DEGs) separated by a barrier. Recent surge of interest in DQW structures can be attributed to the fact that DQWs display richer unique physical properties than single QWs due to an extra degree of freedom in the growth direction ($\| \mathbf{z}$). Some of the examples are the interlayer Coulomb-drag effect [1] in zero field, the tunneling Coulomb gap [2], the interlayer-tunneling excitonic effect [3] in strong perpendicular fields $\mathbf{B}_{\perp}$, and 2D-2D interwell tunneling in $B_{||}$ [4-8]. In DQWs, one can control the well-to-well separation and the interwell overlap, both sensitive to the barrier thickness. The charges in the wells can be controlled by gate voltages. We show that $B_{||}$ provides an additional control of the effective interwell coupling by displacing the wave vectors $\mathbf{k}$ in the two QWs. As a result, $B_{||}$ can be used to tune the tunneling current and deform the Fermi surface, introducing sharp $B_{||}$-dependent structures in the density of states (DOS) and other in-plane transport properties [9-13]. In contrast to the high $\mathbf{B}_{\perp}$ case [2, 3], Coulomb interactions are used in $\mathbf{B}_{||}$ only for band bending corrections and can otherwise be neglected: our data are well explained using the combined effect of tunneling and $B_{||}$ within the frame work of noninteracting electrons. Three samples discussed in this paper are symmetric (except for sample 1) GaAs/$Al_{0.3}Ga_{0.7}As$ DQWs with well widths w and depths V_0. The GaAs wells are separated by an $Al_{0.3}Ga_{0.7}As$ barrier of thickness t.

The primary effect of $\mathbf{B}_{||}$ is to induce a linear transverse displacement $\Delta k_y \propto B_{||}$ in k-space in one QW relative to the other. Here the in-plane wave vector $\mathbf{k}$ is a good quantum number. The linear displacement arises from the second term of the Hamiltonian:

$$H = \frac{p_z^2}{2m^*} + \frac{\hbar^2}{2m^*}(k_y - \frac{z}{\ell^2})^2 + V(z), \qquad (1)$$

DISCLAIMER

DISCLAIMER

Portions of this document may be illegible in electronic image products. Images are produced from the best available original document.

where $p_z = -i\hbar\partial/\partial z$ and $\ell = (\hbar c/eB_{||})^{1/2}$. The GaAs effective mass $m^* = 0.067$ (in units of the free electron mass) is used in both the QWs and the barriers because the confinement wave functions $\phi_n(z)$ (n = 1, 2) penetrate negligibly into the barriers. The kinetic energy $\varepsilon(k_x) = (\hbar k_x)^2/2m^*$ is to be added to (1). The confinement potential $V(z)$ is a superposition of the potentials $V_1(z)$ and $V_2(z)$ of QW1 and QW2. We assume quasi-2D (i.e., $w < \ell$) thin QW's where only the ground sublevels are populated and are relevant. For the sake of physical argument and for 2D-2D tunneling in Sec. 2, z in the second term of (1) can be replaced by its expectation values $\langle z\rangle_1$, $\langle z\rangle_2$ with respect to $\phi_n(z)$ [6]. The net effect of $B_{||}$ is then to shift the origin of k_y of QW2 by $\Delta k_y = d / \ell^2 \propto B_{||}d$ relative to that of QW1, where $d = \langle z\rangle_2 - \langle z\rangle_1$. The basic transport properties to be discussed in the following arise from the $B_{||}$-induced shift Δk_y and the tunneling between the two QWs. Spin splitting is neglected in this paper.

2. Resonant 2D-2D tunneling

The tunneling conductance G_{zz} is the steady-state current flowing from QW1 to QW2 per unit linear electric field applied between the QWs. The current flows into QW1 from a source, tunnels into QW2, and then flows out of QW2 to the drain. The source-drain resistance is related to the tunneling conductance and the zero-$B_{||}$ conductances (i.e., mobilities) of the QWs in terms of a transmission-line model [6,7]. The G_{zz} data is obtained from the source-drain resistance data using this relationship [7]. The latter depends on the geometrical structure of the source-drain current paths of the sample [6]. The electrons are rapidly scattered inside the QWs, occasionally tunnelling into the other QW with the tunneling integral J. A weak dependence of J on $\mathbf{k}$ is ignored [6]. For tunneling from $\mathbf{k}$ in QW1 to $\mathbf{k}'$ in QW2 (with $k = |\mathbf{k}|$ and the sublevel energy Δ_n), the initial and final energies are given by

$$\varepsilon_{1\mathbf{k}} = \frac{(\hbar k)^2}{2m^*} + \Delta_1, \quad \varepsilon_{2\mathbf{k}'} = \frac{(\hbar k_x')^2}{2m^*} + \frac{\hbar^2(k_y' - \Delta k_y)^2}{2m^*} + \Delta_2. \tag{2}$$

Only the electrons on the Fermi circles can tunnel when the energy and momentum conservations are satisfied: $\varepsilon_{1\mathbf{k}} = \varepsilon_{2\mathbf{k}'}$ and $\mathbf{k} = \mathbf{k}'$ [5]. For 2D densities $N_1 > N_2$, the Fermi surfaces are concentric circles of radii k_1 and k_2 at $B_{||} = 0$ as illustrated in the inset of Fig. 1(a) and the conservation conditions are not satisfied. As $B_{||}$ is increased, the inner smaller circle slides relative to the outer circle until they touch each other tangentially. The conservation conditions are satisfied at this $B_{||}$, yielding a G_{zz} peak. As $B_{||}$ is increased further, the inner circle begins to move outside the larger circle, intersecting it at two points. G_{zz} begins to decrease as the area of contact decreases. Another G_{zz} maximum is reached at a higher $B_{||}$, when the smaller circle touches the larger circle from outside. G_{zz} begins to drop beyond this field as the two circles are separated as illustrated in Fig 1(b). The G_{zz} maxima diverge in the absence of scattering. However, the data from sample 1 displayed in Fig. 1(a) does not show the divergence due to finite scattering times as will be shown below. Sample 1 is weakly coupled and has $w = 150$ Å, $t = 65$ Å, $N_1 = 1.8\times10^{11}$ cm^{-2}, and $N_2 = 1.0\times10^{11}$ cm^{-2}.

The tunneling conductance is calculated using a linear response theory. The dominant contribution arises from the so-called bubble diagram shown in Fig. 1(b) and is given by [6]

$$G_{zz} = \frac{4\pi e^2}{\hbar} J^2 \sum_{\mathbf{k}} \int_{-\infty}^{\infty} [-f'(\zeta)] \rho_{1\mathbf{k}}(\zeta) \rho_{2\mathbf{k}}(\zeta) d\zeta, \tag{3}$$

where $f'(\zeta)$ is the first derivative of the Fermi function $f(\zeta)$ and

$$\rho_{n\mathbf{k}} = \frac{1}{\pi} \frac{\Gamma_n}{(\zeta - \varepsilon_{n\mathbf{k}})^2 + \Gamma_n^2}. \tag{4}$$

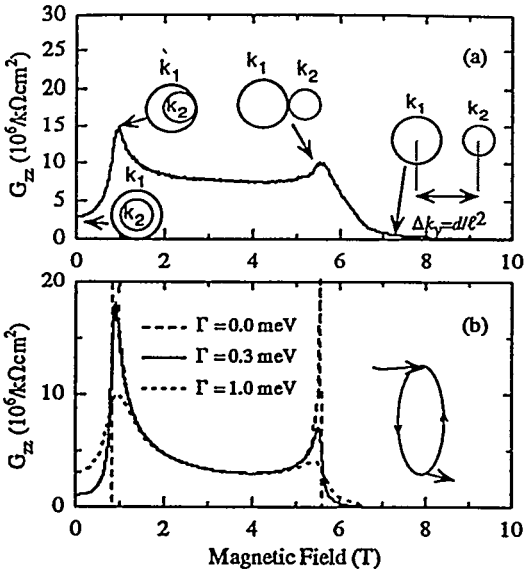

Figure 1. Tunneling conductance per unit area from the data from sample 1 (a) and theory (b). The insets show the relative Fermi surfaces of the QWs (a) and the bubble diagram (b).

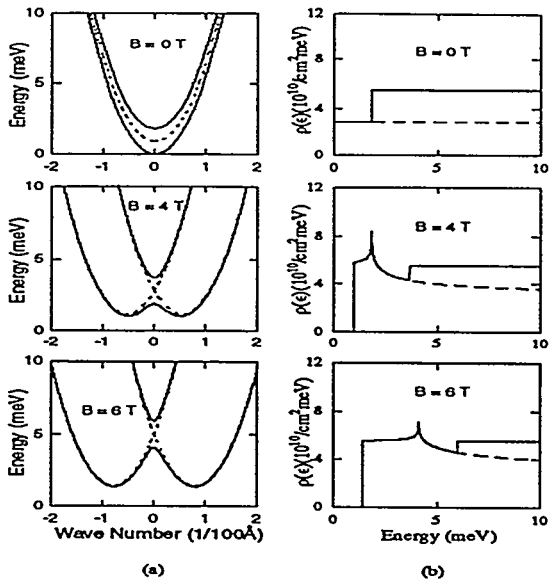

Figure 2. (a) Energy dispersion curves from sample 2 with (solid curves) and without (dashed curves) tunneling. (b) The DOS from the lower (dashed curves) and both branches (solid curves).

Here $\tau_n = (2\Gamma_n/\hbar)^{-1}$ is the quantum scattering time of the electrons on the Fermi surface.

The mobilities in the wells are $\mu_1 = 6\times10^4$ cm^2/Vs and $\mu_2 = 6\times10^5$ cm^2/Vs, indicating that $\Gamma_1 >> \Gamma_2$. In this case, G_{zz} becomes independent of Γ_2. The theoretical G_{zz} displayed in Fig. 1(b) for several values of Γ_1 and $J = 0.04$ meV, show good agreement with the data. This value of J is close to $J = 0.03$ meV estimated from the splitting of the two ground sublevels due to tunneling. For isotropic scattering, the mobility $\mu_1 = 6\times10^4$ cm^2/Vs corresponds to Γ_1 = 0.15 meV and $\tau_1 = 2.3\times10^{-12}$ s. The G_{zz} maxima diverge for $\Gamma_1 = 0$ at the fields $B_\pm = \hbar c\sqrt{2\pi}(\sqrt{N_>} \pm \sqrt{N_<})/ed$, where $N_>$ ($N_<$) is the larger (lesser) of N_1 and N_2.

3. In-plane transport properties

3.1. Energy dispersion and anticrossing

DQW structures show interesting in-plane transport properties when interwell tunneling is significant. The $B_\parallel$-induced linear displacement $\Delta k_y \propto B_\parallel$ of the origins of the transverse crystal momenta k_y in the two QWs is shown in Fig. 2(a) by dashed curves for sample 2 which has $w = 150$ Å, $t = 25$ Å, and $N_1 = N_2 = 1.5\times10^{11}$ cm^{-2}. For such a thin barrier (i.e., large orverlap) between the QWs, the two energy-dispersion parabolas anticross significantly and a partial minigap is formed as shown by the solid curves therein. For symmetric DQWs, the latter correspond to the upper and lower branches of the eigenvalues of (1) (to the lowest order in the overlap $\langle\phi_1(z)|\phi_2(z)\rangle$) [9, 13]:

$$\varepsilon_\pm(k_y) = \varepsilon(k_y) + \frac{d_1^2 + (\Delta z_1)^2}{\ell^2}\varepsilon_\ell \pm \left(4\varepsilon_\ell\varepsilon(k_y)d_1^2/\ell^2 + (\frac{E_g}{2})^2\right)^{1/2} + \frac{E_g}{2}, \tag{5}$$

where $\varepsilon(k_y) = (\hbar k_y)^2/2m^*$, $\varepsilon_\ell = (\hbar\ell^{-1})^2/2m^*$, $d_n = |\langle z\rangle_n|$, and $d_1 = d_2$. Here $(\Delta z_n)^2 = \langle\phi_n(z)|(z - \langle z_n\rangle)^2|\phi_n(z)\rangle$ is the mean square deviation of z arising from finite widths of the QWs. In (5), use is made of $\Delta z_1 = \Delta z_2$. The minigap is independent of $B_\parallel$ and is given by

$$E_g = 2|S_{12}\langle\phi_1(z)|V_2(z)|\phi_1(z)\rangle - \langle\phi_1(z)|V_1(z)|\phi_2(z)\rangle|. \tag{6}$$

Square-well potentials are used for the curves in Fig. 2. A similar anticrossing of dispersion curves, although of different origin occurs without $B_{||}$'s in a vicinal surface such as (911) of a Si-inversion layer and was studied extensively many years ago [14].

3.2. Minigap and density of states

The lower minigap edges in Fig. 2(a) at 4 T and 6 T are saddle points with opposite signs of curvatures in the k_x and k_y directions. The DOS has a van Hove singularity diverging logarithmically at the saddle point as shown in Fig. 2(b) at these $B_{||}$'s. The latter is formed only at high fields (i.e., $B_{||} = 4$ T) when the energy of the crossing point is large enough to overcome the energy repulsion between the two branches. The sharp step in the DOS in Fig. 2(b) is due to the contribution from the upper branch. The region between the sharp singularity and the step is the minigap and moves up in energy rigidly with increasing $B_{||}$ as shown in Fig. 2(b). For the samples discussed in this paper, the 2D density $N_{2D} = N_1 + N_2$ is sufficiently high so that the chemical potential μ lies in the upper branch (i.e., above the step edge) at $B_{||} = 0$. At low $B_{||}$'s, μ is insensitive to $B_{||}$ while the gap rises in energy nearly quadratically with $B_{||}$ [9]. Therefore the gap sweeps through μ as $B_{||}$ is increased. Above these $B_{||}$'s, μ rises in energy eventually together with the bottom of the lower branch. In Fig. 3, we compare the calculated reduced DOS at μ with the capacitive DOS data [15] from sample 3 in units of $m^*A/(2\pi\hbar^2)$, where A is the cross-sectional area of the QWs. Use is made of $d = 140$ Å, $(\Delta z_1)^2 = 621$ Å^2 obtained by a self-consistent Hartree approximation, and $E_g = 1.8$ meV determined experimentally from the conductance data [10]. The latter is somewhat smaller than the Hartree value $E_g = 2.0$ meV. Sample 3 has $w = 100$ Å, $t = 35$ Å, and $N_{2D} = 2.4\times10^{11}$ cm^{-2}. μ drops off the DOS step suddenly at ~7.2 T and passes through the saddle point at ~ 8.9 T. Sharp edges as well as the singularity peak are rounded by damping [15]. The data are fitted at the theoretical asymptotic value $D(\mu) = 2$ at high $B_{||}$'s, where the two QWs are uncoupled. Small oscillations in the data are due to a small $B_{\perp}$.

3.3 Cyclotron mass

The cyclotron mass m_c is given by $m_c = (\hbar^2/2\pi)\partial S/\partial\varepsilon_F$ where S is the orbit area in k-space and ε_F is the Fermi energy [13]. In 2D structures, m_c can be rewritten as $m_c / m^* = D(\mu)$, where $D(\mu)$ is the reduced DOS at the Fermi level from the orbit under consideration. In Fig. 4, we display m_c / m^* calculated for sample 2 using $d = 200$ Å, $(\Delta z_1)^2 = 1150$ Å^2 obtained by a self-consistent Hartree approximation, and $E_g = 1.2$ meV determined experimentally from the conductance data [10]. The latter is somewhat smaller than the Hartree value $E_g = 1.4$ meV. At low $B_{||}$'s, μ is above the gap and the cyclotron orbits consist of a large hour-glass orbit in the lower branch and a smaller lens orbit in the upper branch shown in the lower left corner of Fig. 4. The electrons in the hour-glass orbit have a large mass as shown by the dash-dotted curve and are scattered before completing a cycle: the oscillations from the lower-mass inner lens orbit are dominant in recent Shubnikov-de Haas measurements [12]. As $B_{||}$ increases, μ moves toward the gap edge in Fig. 2(b). As a result, the reduced DOS (i.e., m_c) from the lower and upper branch increases (dash-dotted curve) and decreases (solid curve) monotonically as a function of $B_{||}$, respectively, for the hour-glass orbit and the lens orbit as shown in Fig. 4. At higher $B_{||}$'s (i.e., above 6.1 T in Fig. 4), μ moves into the gap, depopulating the lens orbit. Therefore m_c increases abruptly to the mass of the hour-glass orbit. At 6.9 T, μ lies at the saddle point. Above this $B_{||}$, the orbit splits into two separated orbits and m_c drops to half. The mass thus saturates to m^* of the uncoupled QWs. The calculated m_c yields excellent agreement with the data from sample 2 without adjustable parameters, as shown in Fig. 4 .

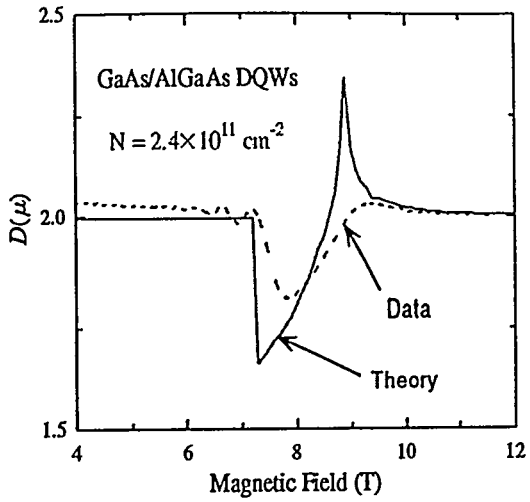

Figure 3. Comparison of the calculated reduced DOS at μ (solid curve) with the capacitive DOS data (dashed curve) from sample 3.

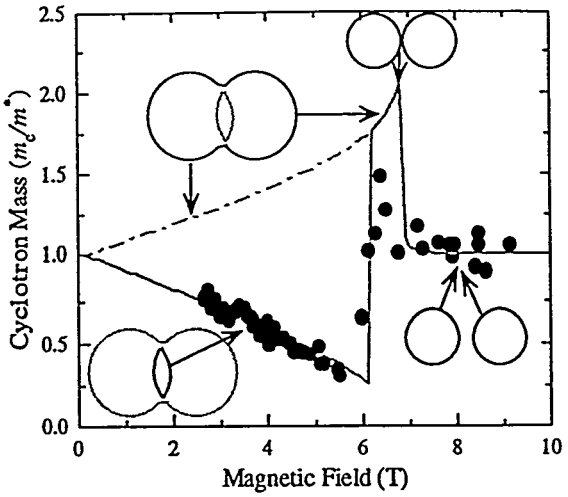

Figure 4. Comparison of the calculated m_c (solid, dash-dotted curves) with the data (black dots) from sample 2 with the relevant cyclotron orbits.

3.3 In-plane conductance

The in-plane conductance $G_{\|}$ in the direction **u** of the electric field is given by [9]

$$G_{\|} = \frac{e^2}{2\pi^2\hbar}\int \tau_{\mathbf{k}} \frac{(\mathbf{u}\cdot\mathbf{v}_{\mathbf{k}})^2}{v_{\mathbf{k}}} dk_{\|}, \tag{7}$$

where $\mathbf{v}_{\mathbf{k}}$ is the group velocity, $v_{\mathbf{k}} = |\mathbf{v}_{\mathbf{k}}|$, $\tau_{\mathbf{k}}$ is the transport relaxation-time, and the integration is along the orbit. We consider only elastic scattering. In (7), $G_{\|}$ is proportional to $v_{\mathbf{k}}$ and $\tau_{\mathbf{k}}$. When μ is above the gap at low $B_{\|}$'s, the contribution to $G_{\|}$ arises from both the hour-glass orbit and the lens orbit in Fig. 4. In contrast to the cyclotron mass, however, the lens orbit contributes little to $G_{\|}$ because 1) the electrons in the lens orbit have slow velocities due to their small k values and 2) the number of states in the lens orbit is much smaller than in the hour-glass orbit. On the contrary, the lens orbit reduces $\tau_{\mathbf{k}}$ and therefore $G_{\|}$ by providing states into which the electrons in the hour-glass orbit are scattered rapidly at low $B_{\|}$'s. As $B_{\|}$ is increased, μ falls below the upper gap edge depopulating the lens orbit. In this case, the electrons in the hour-glass orbit cannot be scattered into the upper branch elastically, yielding significantly larger $\tau_{\mathbf{k}}$ as well as $G_{\|}$. This behavior is shown by the solid curve (i.e., $\Gamma_0 = 0$ meV) in Fig. 5, where we plot $G_{\|}$ calculated for sample 2 by approximating $\tau_{\mathbf{k}} \propto \rho(\varepsilon)^{-1}$ in (7). Here $\rho(\varepsilon)$ is the total DOS. The maximum in $G_{\|}$ is due to the depopulation of the lens orbit. The $G_{\|}$ minimum, on the other hand, arises when μ lies on the saddle point, where $G_{\|}$ vanishes because $\tau_{\mathbf{k}} \propto \rho(\varepsilon)^{-1} = 0$ due to the divergence of the DOS. E_g can be determined from the $B_{\|}$'s of the $G_{\|}$ maximum and minimum [10]. The effect of band bending is to increase the effective d from 175 Å to 200 Å by pushing the confinement wave functions away from each other. Since $B_{\|}$ enters the Hamiltonian approximately as $d/\ell^2 \propto B_{\|}d$, the net effect of band bending is to rescale the $B_{\|}$-axis by $175\times B_{\|}/200$ as shown in the upper axis of Fig. 5. The effect of damping has been treated by a self-consistent linear response theory [16] and is shown in Fig. 5. The calculated results yield good agreement with the data [10] displayed in Fig. 6.

4. Summary

We have discussed low-temperature tunneling and in-plane transport properties in double

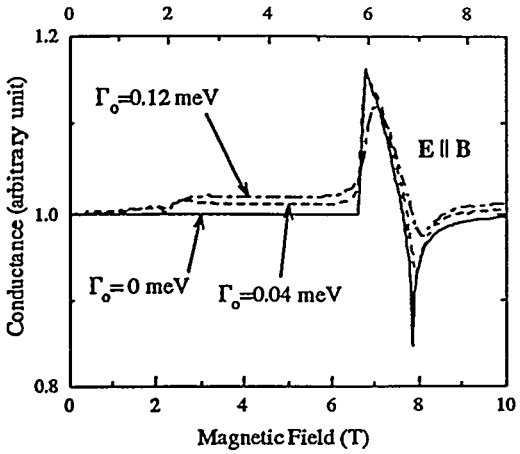

Figure 5. Calculated $G_{||}$ for sample 2 for several values of damping $\Gamma = 2\Gamma_0$. The upper and lower scales are with and without band bending.

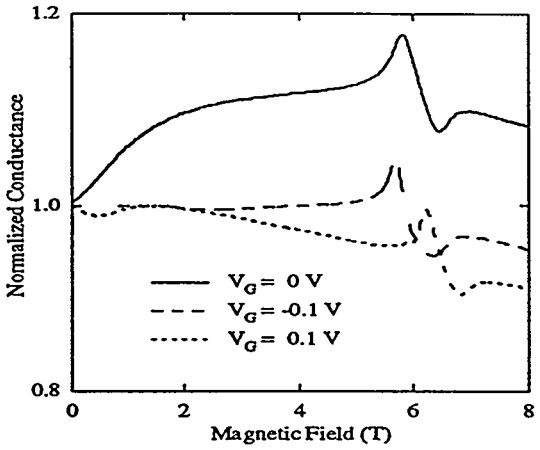

Figure 6. $G_{||}$ data from sample 2. Charges are approximately balanced at the gate bias V_G = -0.1 V.

quantum wells in $B_{||}$'s. These properties arise from the combined effect of $B_{||}$-induced relative displacement of the wave vectors in the two QWs and the interwell tunneling. In weakly coupled DQWs, the interwell tunneling conductance has two sharp maxima as a function of $B_{||}$. In strongly coupled DQWs, a partial minigap is formed due to the anticrossing of the two QW dispersion curves, yielding sharp $B_{||}$-dependent structures in the density of states, cyclotron mass, and the in-plane conductance. Excellent agreement is obtained between the theory and the data from GaAs/AlGaAs DQWs.

This work was supported by the Office of Basic Energy Sciences, Division of Materials Sciences, U. S. DOE under Contract No. DE-AC04-94AL8500.

References

[1] Gramila T J, Eisenstein J P, MacDonald A H, Pfeiffer L N, and West K W1990 Phys. Rev. Lett. **66** 1793-6
[2] Eisenstein J P, Pfeiffer L N, and West K W 1992 Phys. Rev. Lett. **69** 3804-7
[3] Eisenstein J P, Pfeiffer L N, and West K W 1995 Phys. Rev. Lett. **74** 1419-22
[4] Smolinar J, Demmerle W, Berthold G, Gornik E, Weimann G, and Schlapp W 1989 Phys. Rev. Lett. **63** 2116-9
[5] Eisenstein J P, Gramila T J, Pfeiffer L N, and West K W 1991 Phys. Rev. B **44** 6511
[6] Lyo S K and Simmons J A 1993 J. Phys.: Condens. Matter **5** L299-L306
[7] Simmons J A, Lyo S K, Klem J F, Sherwin M E, and Wendt J R 1993 Phys. Rev. B **47** 15741-4
[8] Zheng L and MacDonald A H 1993 Phys. Rev. B **47** 10619-24
[9] Lyo S K 1994 Phys. Rev. B **50** 4965-8
[10] Simmons J A, Lyo S K, Harff N E, and Klem J F 1994 Phys. Rev. Lett. **73** 2256-9
[11] Kurobe A, Castleton I M, Linfield E H, Grimshaw M P, Brown K M, Ritchie D A, Pepper M, and Jones G A C 1994 Phys. Rev. B **50** 4889-92.
[12] Simmons J A, Harff N E, and Klem J F 1995 Phys. Rev. B **51** 11156-9
[13] Lyo S K 1995 Phys. Rev. B **51** 11160-3
[14] Ando T, Fowler A B, and Stern F 1982 Rev. Mod. Phys. **54** 437-672
[15] Eiles T M, Simmons J A, Lyo S K, Harff N E, and Klem J F, unpublished.
[16] Lyo S K, Simmons J A, and Harff N E, 1995 *The Physics of Semiconductors: Proceedings of the 22nd International Conference, Vancouver, 1994, Vol. 1, 843-6*, edited by D. J. Lockwood (World Scientific, Singapore)